OPTICS

On-chip mechanical exceptional points based on an optomechanical zipper cavity

Ning Wu[1,2]†, Kaiyu Cui[1,2]*†, Qiancheng Xu[1,2], Xue Feng[1,2], Fang Liu[1,2], Wei Zhang[1,2,3], Yidong Huang[1,2,3]*

Exceptional points (EPs) represent a distinct type of spectral singularity in non-Hermitian systems, and intriguing physics concepts have been studied with optical EPs recently. As a system beyond photonics, the mechanical oscillators coupling with many physical systems are expected to be further exploited EPs for mechanical sensing, topology energy transfer, nonreciprocal dynamics, etc. In this study, we demonstrated on-chip mechanical EPs with a silicon optomechanical zipper cavity, wherein two near-degenerate mechanical breathing modes are coupled via a single colocalized optical mode. By tailoring the dissipative and coherent couplings between two mechanical oscillators, the spectral splitting with 1/2 order response, a distinctive feature of EP, was observed successfully. Our work provides an integrated platform for investigating the physics related to mechanical EPs on silicon chips and suggests their possible applications for ultrasensitive measurements.

INTRODUCTION

The non-Hermitian system, which exchanges energy with the outside environment, is quite different from the conservative Hermitian system. Exceptional points (EPs) are special degenerate points of spectra that exist in the non-Hermitian system. For *N*th-order EPs, *N* eigenvalues and eigenvectors coalesce simultaneously at the EPs, and the theorem of completeness and orthogonality fails in this system (*1*–*4*). Thus, owing to this characteristic, intriguing physics concepts are expected. In the past few years, optical EPs have been demonstrated in various platforms including optical and microwave cavities (*5*–*9*), photonic crystal slabs (*10*), and multilayered plasmonic structures (*11*). Furthermore, certain counterintuitive phenomena have been reported and observed experimentally (*1*–*4*). For instance, when a small disturbance of strength ε acts on the EPs, spectral splitting is proportional to $\varepsilon^{1/N}$. As a result, for a 1/*N* order response, the spectral splitting near the EPs may be far greater than the normal mode splitting in the Hermitian system, where splitting of degenerate points is proportional to the perturbation ε. This property was used to improve the performance of the single-mode operation in multimode laser cavities (*12*) and enhance the sensitivities of sensors (*5*, *11*, *13*–*15*). In addition, encircling the EPs in parameter space is nonreciprocal and the counterclockwise evolution is distinct from the clockwise one. This effect was demonstrated in topology energy transfer (*16*, *17*) and asymmetric mode switching (*18*). However, studies to date have focused primarily on optical EPs. The EPs in other physical systems are expected to be exploited further.

In cavity optomechanics, mechanical properties such as resonant frequency and dissipation rate can be adjusted effectively via optical modes through radiation pressure. Moreover, the mechanical and optical modes coupled with the thermal bath constitute a natural non-Hermitian system. Although this system is promising for manipulating mechanical modes and achieving mechanical EPs in multiphysics systems, experimental studies on mechanical EPs are still very limited (*16*, *17*, *19*). Fully integrated mechanical EPs have remained elusive because of great challenges in on-chip mechanical manipulation.

In this study, we demonstrate on-chip mechanical EPs in an optomechanical zipper cavity at ambient environment, wherein two near-degenerate gigahertz mechanical breathing modes are coupled via a colocalized single optical mode. In this experiment, the strength of dissipative and coherent couplings between two mechanical oscillators is controlled by adjusting the frequency and power of the pump light to compensate for the difference of complex frequencies between the two mechanical breathing modes. Accordingly, the topology surface near the mechanical EP was mapped and a spectral splitting with 1/2 order response, a distinctive feature of EPs, was observed. As nanomechanical resonators can be coupled with many physical systems (*20*) and are suitable for detecting quantities such as mass, charge, and torque (*21*–*23*), our work paves the way for high-sensitivity measurement with mechanical EPs on integrated platforms. Moreover, this research sets the foundation for studying the related physics of mechanical EPs and other non-Hermitian phenomena based on optomechanical crystals.

RESULTS

Mechanical EPs based on multimode optomechanical coupling can be analyzed as two independent pendulums with different oscillation frequencies (two mechanical modes) interacting with an optical mode in a Fabry-Perot cavity constructed by the two pendulums, as shown schematically in Fig. 1A. The optical mode acts as a bridge that connects the two mechanical modes. The oscillation of each pendulum can modulate the resonant frequency of the optical mode; thus, subsequently, the light intensity in the cavity changes. Accordingly, the oscillation of radiation pressure force that originates from the variation of light intensity in the cavity affects the motion of the other pendulum and thereby enables the coupling

[1]Department of Electronic Engineering, Tsinghua University, Beijing 100084, China. [2]Beijing National Research Center for Information Science and Technology (BNRist), Tsinghua University, Beijing 100084, China. [3]Beijing Academy of Quantum Information Sciences, Beijing, China.
*Corresponding author. Email: kaiyucui@tsinghua.edu.cn (K.C.); yidonghuang@tsinghua.edu.cn (Y.H.)
†These authors contributed equally to this work.

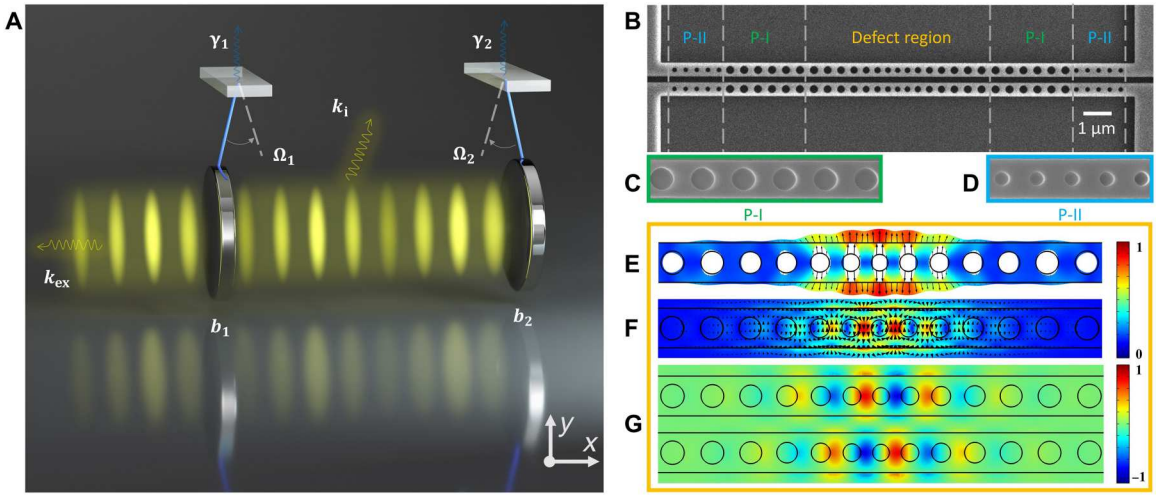

Fig. 1. The proposed optomechanical zipper cavity and its physical model. (**A**) Schematic of a Fabry-Perot cavity that consists of two pendulums as the reflecting mirror that act as mechanical modes b_1 and b_2 with oscillation frequency, Ω_1 and Ω_2, and are coupled to the thermal bath at the rate of γ_1 and γ_2, respectively. The optical mode of the Fabry-Perot cavity loses energy via the intrinsic loss channel at rate k_i and detectable extrinsic coupling channel at rate k_{ex}. (**B**) Scanning electron microscope (SEM) image of silicon optomechanical zipper cavity. Magnified SEM image of (**C**) periodic structure in P-I region and (**D**) periodic structure in P-II region. (**E**) Displacement field |**u**| of the breathing mode simulated with the finite element method (FEM) in one arm of the optomechanical zipper cavity. FEM simulation of (**F**) electric field |**E**| of first-order optical mode in a single nanobeam cavity and (**G**) electric field E_y component of first-order odd optical mode in zipper cavity. (E and F) Black arrows represent the field directions of the mechanical displacement field and the electric field on the top surface of the silicon structure. u_y and E_y are the main components of the mechanical displacement field and electrical field, respectively. The optomechanical coupling mainly originates from the overlap between the strain component $S_{yy} = \partial u_y/\partial y$ (*33*) and the electric field component E_y in this structure.

between the two mechanical modes. Note that the coupling here is distinct from mode coupling in the Hermitian system. In a Hermitian system, one of the mechanical oscillators exerts a force proportional to its displacement on another oscillator and leads to the coherent coupling (*24*–*26*). When the coherent coupling rate is enhanced, the normal mode splitting increases. However, for the non-Hermitian optomechanical system, in addition to the coherent coupling, the force exerted by one of the mechanical oscillators on the other also contains the dissipative coupling (*27*), which results in a notable change in the physical scenario. The corresponding quantitative description is as follows.

The coupling strength between the mechanical oscillators, including both the coherent and dissipative couplings, is primarily controlled by the optical mode. When a pump laser with frequency ω_L drives the optical mode with resonance frequency ω_{cav}, detuning $\Delta = \omega_L - \omega_{cav}$ and intracavity photon number n_{cav} can be adjusted by changing the frequency ω_L and power P_{in} of the pump laser. To further quantitatively describe the relationship between these parameters and the dynamics of the model shown in Fig. 1A, the Heisenberg-Langevin equations (*28*) are solved in the frequency domain (section S1), and the effective Hamiltonian of the mechanical oscillators can be expressed as

$$H_{\text{eff}} = \begin{bmatrix} \Omega_1 - i\gamma_1/2 + g_1^2\chi & g_1g_2\chi \\ g_1g_2\chi & \Omega_2 - i\gamma_2/2 + g_2^2\chi \end{bmatrix}$$

where $\chi \approx n_{cav}\{1/[(w + \Delta) + ik/2] - 1/[(w - \Delta) + ik/2]\}$ and $w = (\Omega_1 + \Omega_2)/2$. k is the optical dissipation rate, and g_j (j = 1, 2) is the vacuum optomechanical coupling rate between the optical mode and the jth mechanical mode. For the diagonal elements of the effective Hamiltonian H_{eff}, mechanical resonant frequencies Ω_1 and Ω_2 are modified owing to the optical spring effect. Meanwhile, the mechanical dissipation rates γ_1 and γ_2 are decreased (increased) by the antidamping (damping) effect of optomechanical coupling when a blue (red) detuned laser (*28*, *29*) is used. Furthermore, the off-diagonal element is a complex number, and its real and imaginary parts correspond to the coherent and dissipative couplings, respectively. The eigenvalues, which characterize the evolution of this two-level system, can be further represented as

$$\begin{aligned} \omega_\pm &= \omega_\pm - i\gamma_\pm/2 \\ &= \frac{1}{2}(\Omega_1 - i\gamma_1/2 + \Omega_2 - i\gamma_2/2) + \frac{1}{2}(g_1^2 + g_2^2)\chi \pm \frac{1}{2}S \end{aligned} \quad (2)$$

where

$$S = \sqrt{[(\Omega_1 - i\gamma_1/2 + g_1^2\chi) - (\Omega_2 - i\gamma_2/2 + g_2^2\chi)]^2 + 4(g_1g_2\chi)^2}$$

Here, the resonant frequencies and mechanical dissipation rates (linewidth) of both mechanical modes are modified by $\frac{1}{2}(g_1^2 + g_2^2)\chi$, and the mode splitting between them is controlled and reflected by parameter S. By tuning parameter χ via sweeping of the detuning Δ and intracavity photon number n_{cav}, the eigenvalue and eigenvector coalesce at the EPs where $S = 0$ when parameter χ satisfies the following condition

$$\chi_{\text{eps}}(\Delta_0, n_{\text{cav}_0}) = \frac{(\Omega_1 - \Omega_2) - i(\gamma_1 - \gamma_2)/2}{g_2^2 - g_1^2 \pm i2g_1g_2} \quad (3)$$

Typically, parameter χ_{eps} is a complex number at the EPs and indicates that the coherent and dissipative coupling mechanisms are both necessary. It can be seen that χ_{eps} is an imaginary number when $g_1 = g_2$ and $\gamma_1 = \gamma_2$, which indicates that the dissipative coupling alone is sufficient to realize the EPs related to anti–parity time symmetry (*30*–*32*) in this situation. Although the hybridization of two mechanical modes was reported recently in the

unresolved-sideband regime ($k >> \Omega$) (*24*–*26*), the dissipative coupling is strongly diminished compared with the coherent coupling in this regime (*28*). As a result, it is crucial to investigate the resolved-sideband regime ($k << \Omega$) of the EPs wherein the coherent and dissipative couplings can be adjusted effectively to compensate for the difference of resonant frequencies and mechanical dissipation rates simultaneously.

When certain disturbances act on a system at the EPs, parameter χ may deviate from χ_{eps}. We define perturbation strength ε as $\varepsilon = \chi - \chi_{eps}$ to characterize the deviation from the EPs. The complex frequency splitting S can be further represented as a function of perturbation ε, $S = \sqrt{|A\varepsilon + B\varepsilon^2|}e^{i\phi}$, where A and B are complex constants and parameter ϕ reflects the ratio of splitting on the real and imaginary parts. For a small disturbance ($B\varepsilon^2 << A\varepsilon$), $|S| \approx \sqrt{|A\varepsilon|}$. In particular, the amplitude of the coefficient A will scale with Ω_1-Ω_2 if $\gamma_1 = \gamma_2$. This implies that a small perturbation ε results in large mode splitting at EPs owing to the 1/2 order response and the large difference of mechanical resonant frequencies.

Following the multimode optomechanical coupling model introduced above, we propose and design the optomechanical zipper cavity, consisting of two identical silicon nanobeam cavities with a 200-nm gap between them, as shown in Fig. 1B. As one arm of the optomechanical zipper cavity, a nanobeam cavity consists of three parts: two quasi-periodic mirror regions (P-I and P-II) and one defect cavity region. The first quasi-periodic structure P-I (Fig. 1C) can avoid optical energy loss via a waveguide as the optical resonant frequency is on the center of the photonic bandgap. The second quasi-periodic structure P-II (Fig. 1D) is used to regulate the mechanical radiation loss when the phononic bandgap is designed properly (section S2). In the defect region, the radius of holes increases gradually from the center moving outward, and both the optical and mechanical modes can be confined (*33*, *34*). We focus on the mechanical breathing mode (Fig. 1E) and the first-order optical mode (Fig. 1F). When two identical nanobeam cavities approach each other to constitute the zipper cavity, the mechanical breathing mode in each nanobeam cavity remains independent of each other. In contrast, the first-order optical degenerate modes in each nanobeam cavity couple to each other through the evanescent field and result in renormalized odd (Fig. 1G) and even optical modes with distinct resonant frequencies. In principle, either of these optical modes can be used to realize the mechanical EPs when it couples to mechanical breathing modes via radiation pressure. In our design, a low optical dissipation rate is required because the system should reach the resolved-sideband regime. Moreover, both high vacuum optomechanical coupling rate g_j and low optical dissipation rate k are expected to decrease the intracavity photon number n_{cav} at EPs and diminish the influence of other nonlinear effects related to light absorption (*35*, *36*). Considering these objectives, the structure parameters such as the radius and pitches of holes were optimized. Last, the designed optical wavelength was λ_{odd} = 1542.5 nm (λ_{even} = 1551 nm), and the optical linewidth was $k/2\pi$ = 0.04 GHz (0.12 GHz) corresponding to optical quality factor $Q_o = 4.86 \times 10^6$ (1.6×10^6). In addition,

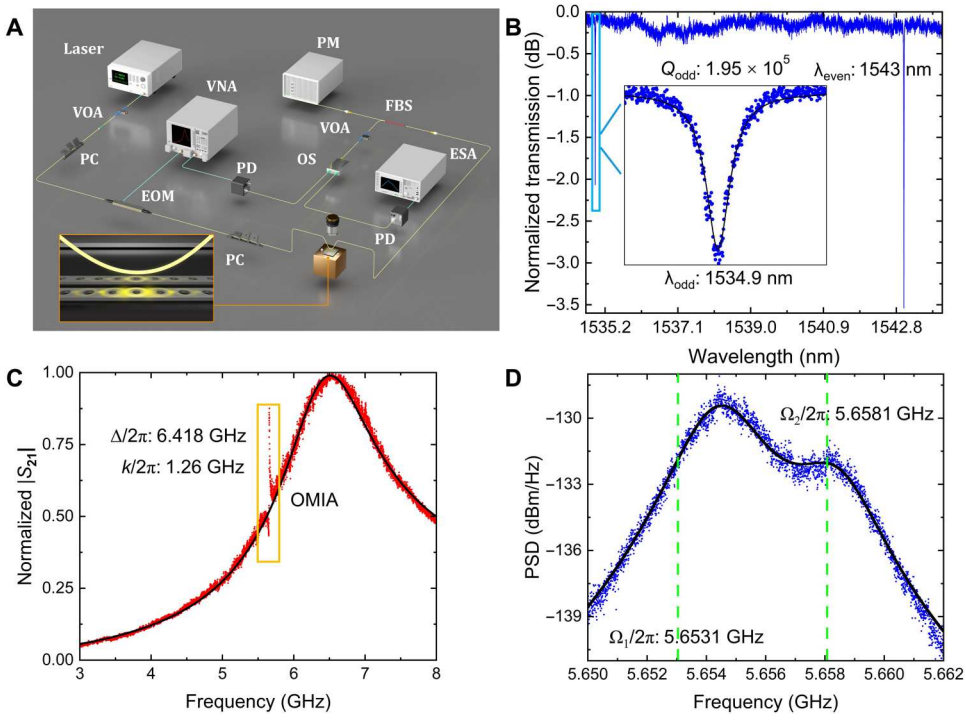

Fig. 2. Characterization of the fabricated optomechanical zipper cavity. (**A**) Experimental setup schematic. VOA, variable optical attenuator; PC, polarization controller; EOM, electro-optic modulator; VNA, vector network analyzer; FBS, fiber beam splitter; PM, power meter; OS, optical switch; PD, photodetector; ESA, electric spectrum analyzer. (**B**) Low–input power optical transmission spectrum. The first (1534.9 nm) and second (1543 nm) resonant dips correspond to odd and even optical modes, respectively. (**C**) Amplitude response of S_{21}. k values at high optical power and detuning Δ are deduced from this response. (**D**) PSD of mechanical spectrum after subtracting the background noise, obtained under the same condition in (C). Green dashed line represents intrinsic resonant frequency of both mechanical oscillators. (B to D) Black solid lines represent fitting results.

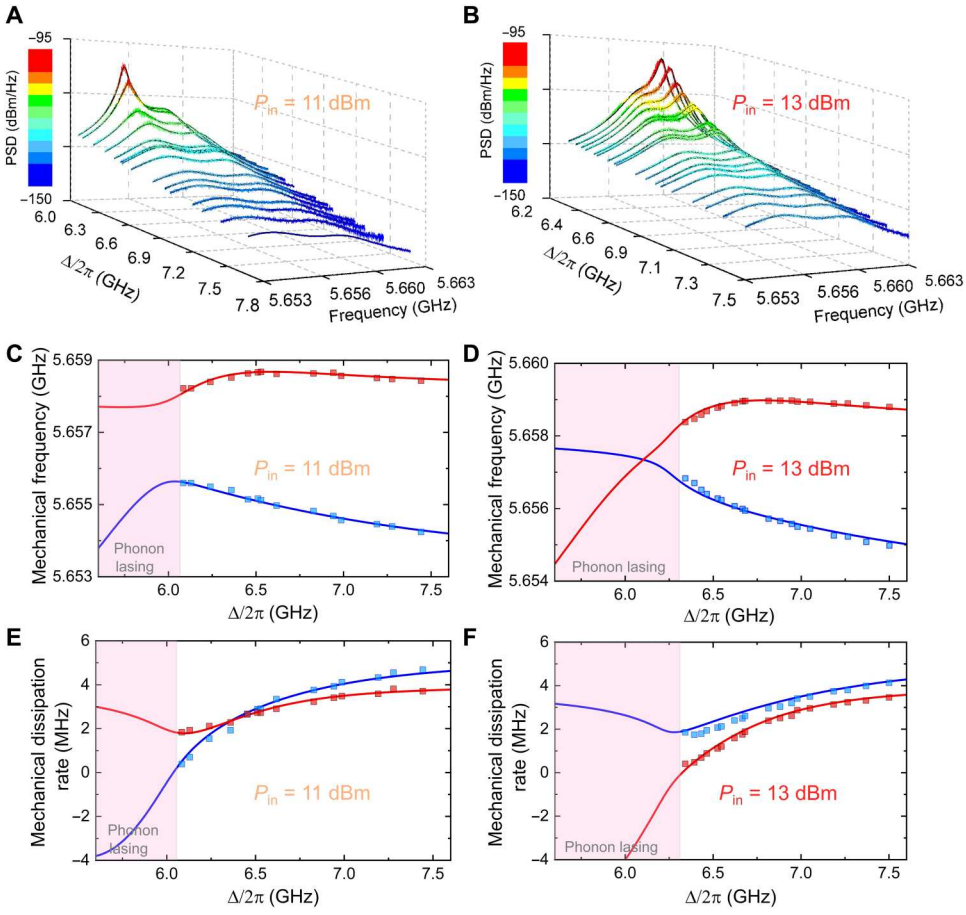

Fig. 3. The evolution of mechanical modes. (**A** and **B**) PSD of mechanical spectra after subtracting the background noise when optical detuning is scanned with fixed laser power P_{in} = 11 dBm and P_{in} = 13 dBm, respectively. Black solid lines represent fit to experimental data. (**C** and **D**) Mechanical resonant frequencies $\omega_{\pm}/2\pi$ versus the optical detuning Δ, deduced from the spectra in (A) and (B), respectively. (**E** and **F**) Mechanical dissipation rate $\gamma_{\pm}/2\pi$ versus the optical detuning Δ, deduced from the spectra in (A) and (B), respectively; (C to F) square markers correspond to fitting results of experimental spectra, and blue and red lines are theoretical results using the linear approximation.

the designed mechanical frequency was $\Omega_1/2\pi = \Omega_2/2\pi = 5.634$ GHz and the optomechanical coupling rate was $g_1/2\pi = g_2/2\pi = 0.63$ MHz.

After determining the parameters of the zipper cavity, the designed cavity was fabricated on a silicon-on-insulator wafer with a top layer thickness of 220 nm and a 3-μm-thick buried-oxide layer (Materials and Methods). Figure 2A shows the measurement setup used to characterize the evolution of mechanical spectra with tuned optical parameters. A tapered fiber controlled with nanopositioners was used to evanescently couple the input blue-detuned laser into the zipper cavity. In this experiment, a pump-probe scheme (*37*–*39*) was used to monitor the detuning Δ and the optical dissipation rate k (section S3).

The optical and mechanical spectra are illustrated in Fig. 2 (B to D). In Fig. 2B, the first resonant dip at 1534.9 nm is an odd optical mode, while the second resonance dip at 1543 nm corresponds to an even optical mode. In this experiment, we excite the optical odd mode to realize the mechanical EPs, and its Lorentzian fitting is shown in the inset. The corresponding optical linewidth of $k/2\pi = 1$ GHz ($Q_o = 1.95 \times 10^5$) indicates that the resolved-sideband regime ($\Omega >> k$) was reached. The derived extrinsic coupling rate of $k_{ex}/2\pi = 0.208$ GHz from Fig. 2B is assumed to be constant during the experiment and was used to calculate the intracavity photon number n_{cav}. The normalized amplitude response of S_{12} (red points in Fig. 2C) detected via the vector network analyzer after calibrating the frequency response (section S4) is consistent with the theoretical fitting (black line), and the optical linewidth and detuning can be derived. Meanwhile, a narrow resonant dip appears when the beat frequency between the pump and weak probe lights is close to the mechanical resonant frequency. This can be attributed to the effect of optomechanical-induced absorption (OMIA) (*39*). Here, with the large n_{cav} inside the cavity, the derived optical linewidth $k/2\pi = 1.26$ GHz is distinct from the result in Fig. 2B because of the nonlinear absorption effect (*35*). The power spectrum density (PSD) in Fig. 2D carrying the information of mechanical motion and the related mechanical mode properties can be deduced by using multiple spectra measured under different detunings and optical input powers. Here, the fitting parameters were as follows: $\Omega_1/2\pi = 5.6531$ GHz, $\Omega_2/2\pi = 5.6581$ GHz, $Q_1 = \Omega_1/\gamma_1 = 1100$, $Q_2 = \Omega_2/\gamma_2 = 1440$, $g_1 = 0.72$ MHz, and $g_2 = 0.32$ MHz. Compared to the intrinsic mechanical resonant frequencies, resonant peaks in Fig. 2D are blue-shifted due to the optical spring effect.

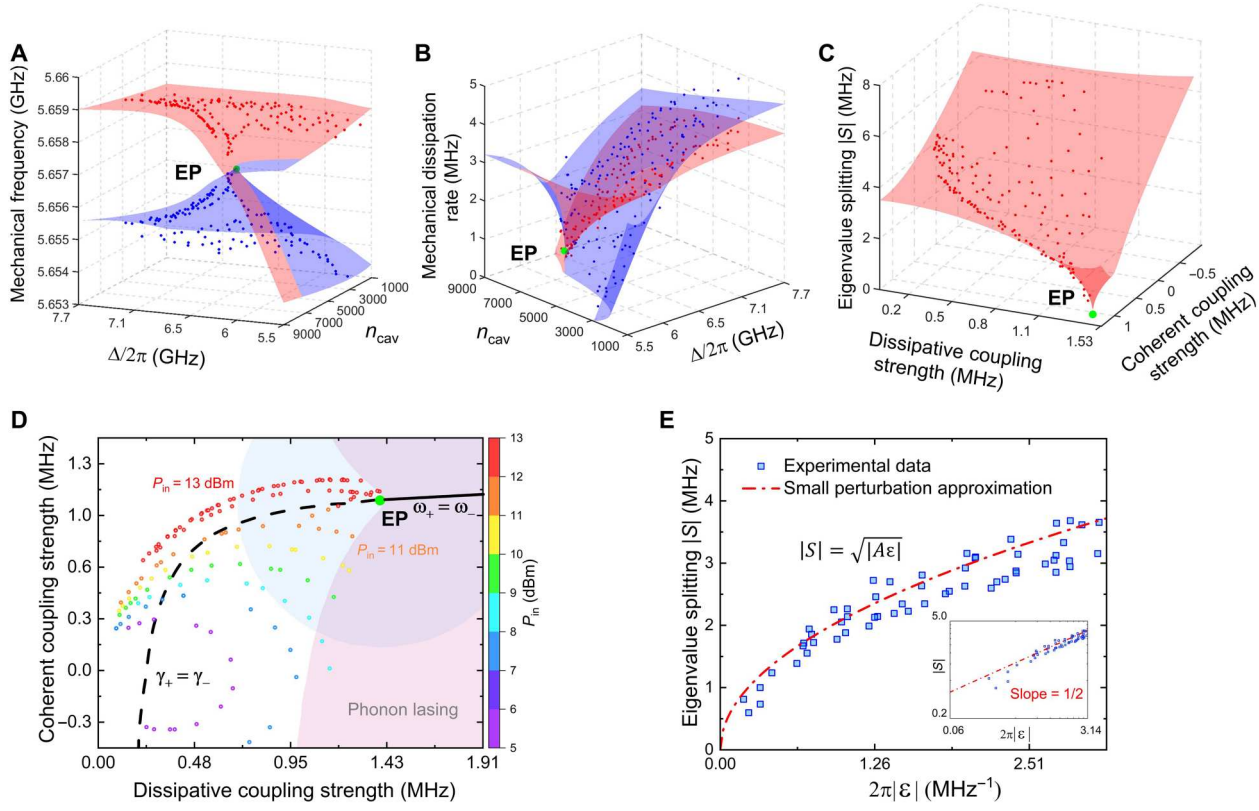

Fig. 4. Characterization of the experimental results near the mechanical EP. (**A**) Resonant frequencies $\omega_{\pm}/2\pi$ and (**B**) dissipation rate $\gamma_{\pm}/2\pi$ of mechanical modes versus detuning Δ and intracavity photon number n_{cav}. (**C**) Amplitude of eigenvalue splitting S versus the dissipative and coherent coupling strength. In (A) to (C), topology surfaces are calculated from the theoretical model using parameters deduced from experimental results. Blue and red points are experimental results. (**D**) Distribution of the experimental data (circle markers) in parameter space. (**E**) Amplitude of eigenvalue splitting S versus amplitude of perturbation ε. Inset shows alternative logarithmic scale presentation where the 1/2 order response corresponds to the line with slope = 1/2. (A to D) Green point corresponds to an EP.

Furthermore, the mechanical peak at higher frequency is weaker than that at lower frequency because the optomechanical coupling rate g_2 is lower. In addition, the discrepancy of the intrinsic resonant frequencies between the two mechanical oscillators originates from the fabrication error and it contributes to a large eigenvalue splitting near the EPs.

To analyze the evolution of the eigenvalue of the mechanical modes with the variation of the detuning Δ and the intracavity photon number n_{cav}, the mechanical spectra are measured by scanning the optical detuning Δ at a fixed laser power P_{in} = 11 dBm and P_{in} = 13 dBm in Fig. 3 (A and B, respectively). For P_{in} = 11 dBm in Fig. 3A, we observed a notable increase in the peak of the mechanical mode with lower frequency as the detuning Δ decreases, which indicates the decrease in the mechanical linewidth. Subsequently, the phonon lasing (*40*–*42*) occurred in this lower-frequency mode. In contrast, for P_{in} = 13 dBm, it can be found that the peak (linewidth) of the mechanical mode with higher frequency shown in Fig. 3B increases (decreases) markedly as the detuning Δ decreases. Thereafter, the phonon lasing occurred in this higher-frequency mode. This phenomenon is also an evidence of the coupling between the two mechanical oscillators. Otherwise, the lower-frequency mode would always enter the phonon lasing regime first because of its higher optomechanical coupling rate g_1.

Furthermore, mechanical eigenvalues $\omega_{\pm} - i\gamma_{\pm}/2$ can be obtained from the mechanical spectra. Figure 3, C and E (Fig. 3, D and F), displays the evolution of the real and imaginary part of eigenvalues for different detuning Δ using the spectra in Fig. 3A (Fig. 3B), respectively. Here, the experimental data (square markers) are consistent with the theoretical curves (solid lines) with the linear approximation. In addition, the crossing (anticrossing) of the dissipation rate $\gamma_{\pm}/2\pi$ and the anticrossing (crossing) of frequency $\omega_{\pm}/2\pi$ of the mechanical modes appear as theoretical prediction when the detuning is swept at P_{in} = 11 (13) dBm. This property can be illustrated in Fig. 4D; here, the black solid (dashed) line corresponds to parameters where the real (imaginary) parts of the eigenvalues are degenerate. As the real and imaginary parts of the mechanical modes are simultaneously degenerate at the EPs, the corresponding parameter point of the EPs is the intersection of the black solid and dashed line. Because of this property of the EPs, under the higher (lower) laser power, the evolution of parameters will cross the black solid (dashed) line when the detuning is swept. Then, the crossing of the mechanical frequency (dissipation rate) of mechanical modes will show up and the phase transition occurs at the EPs. Nevertheless, the system enters the phonon lasing regime before the frequency crossing at P_{in} = 13 dBm experimentally in Fig. 3 (D and F), owing to the low intrinsic mechanical dissipation rate of this test sample. Accordingly, the evolution of mechanical spectra will deviate from the theoretical curve with a linear approximation, and the relation between the coupling strength (coherent and dissipative coupling) and the optical

parameters (n_{cav} and Δ) will change. Even so, the relation between the eigenvalues and the coupling strengths (coherent and dissipative coupling) will maintain and will still be effective to analyze the results in the phonon lasing regime (section S7). Thus, in the phonon lasing regime, the coherent and dissipative coupling strength will be saturated until the imaginary part of the eigenvalue for the phonon lasing mode becomes zero and a lasing frequency is exactly one of the real parts of system eigenvalues to satisfy the system dynamics. Moreover, the crossing and the anticrossing properties will still have the corresponding consequences after the transition from the linear to the phonon lasing regime (section S7).

Following the abovementioned procedure, we further reconstruct the topological surface of the mechanical eigenvalues under different laser powers and detuning. The mechanical resonant frequency $\omega_{\pm}/2\pi$ and the mechanical dissipation rate $\gamma_{\pm}/2\pi$ versus the detuning Δ and intracavity photon number n_{cav} are plotted in Fig. 4 (A and B, respectively). Figure 4C shows the amplitude of mode splitting S versus the coherent and dissipative coupling strength to combine the information in Fig. 4 (A and B) and better locate the EP. It can be seen that the experimental data (blue and red points) are consistent with the theoretical surface results, and the region near the EPs was reached. Here, the relation between optical dissipation rate k and intracavity photon number n_{cav} has been considered in the theoretical calculation (section S5), and the deviation between the experimental data and the theoretical surface mainly comes from the long-term drift of the intrinsic mechanical frequency (section S6).

Then, we focus on the variation of eigenvalues near the EPs. According to the theoretical model, the amplitude of mode splitting S is a nonlinear function of the perturbation ε, where $|S| = \sqrt{|A\varepsilon + B\varepsilon^2|}$. As the experimental data are close to the EPs in the parameter space, the perturbation ε can be very small. This leads to a good agreement between the corresponding experimental eigenvalue splitting for the data inside the blue circle in Fig. 4D and the approximate theoretical response of $|S| = \sqrt{|A\varepsilon|}$, as illustrated in Fig. 4E. Consequently, the 1/2 order response of the EPs was observed in this test sample. In addition, as the amplitude of perturbation ε is a nonlinear function of detuning Δ, the 1/2 order response and the nonlinear transduction between perturbation ε and detuning Δ resulted in a sudden change of mechanical frequency splitting near the EPs in Fig. 4A when the detuning Δ is adjusted.

DISCUSSION

In our experiment, a larger difference of mechanical frequency $|\Omega_1 - \Omega_2|$ will further enhance the frequency splitting near the EPs. In addition, the device also benefits from the reduced mechanical linewidth by using a blue-detuned laser. What is more, owing to the self-reference detection scheme of frequency splitting, this system is robust to mechanical frequency drifts (*43*). In contrast, the sensor proposed by a single optomechanical coupling suffers from frequency drift (*44*, *45*). Therefore, the device is suitable for realizing high-sensitivity sensors by combining the antidamping modes and the mechanical EPs. It is noted that this work also offers a reliable, integratable platform for studying and using multimode non-Hermitian physics. For instance, further using the red detuning laser might be suitable for the investigation of multimode optomechanical cooling (*46*) and the nonreciprocal dynamics of mechanical EPs (*17*, *19*) under the quantum ground state as the high frequency of mechanical breathing modes results in low thermal phonons. In addition, high-order EPs (*47*) and the multimode dynamics in the phonon lasing regime (*48*, *49*) can also be explored further based on this platform.

MATERIALS AND METHODS

Fabrication process of zipper cavity

The designed cavity was fabricated on a silicon-on-insulator wafer with a top layer thickness of 220 nm and a 3-μm-thick buried-oxide layer. Electron-beam lithography was used to define the pattern on resist, and inductively coupled plasma reactive ion etch was used to transfer the pattern to the top silicon layer. Subsequently, the buried-oxide layer was removed using buffered hydrofluoric acid to form the suspended nanobeam structure (*42*, *50*). The fabrication process of the zipper cavity is shown in fig. S2.

Supplementary Materials

This PDF file includes:

Sections S1 to S7
Figs. S1 to S9
References

REFERENCES AND NOTES

1. M.-A. Miri, A. Alù, Exceptional points in optics and photonics. *Science* **363**, eaar7709 (2019).
2. Ş. K. Özdemir, S. Rotter, F. Nori, L. Yang, Parity–time symmetry and exceptional points in photonics. *Nat. Mater.* **18**, 783–798 (2019).
3. R. El-Ganainy, K. G. Makris, M. Khajavikhan, Z. H. Musslimani, S. Rotter, D. N. Christodoulides, Non-Hermitian physics and PT symmetry. *Nat. Phys.* **14**, 11–19 (2018).
4. H.-Z. Chen, T. Liu, H.-Y. Luan, R.-J. Liu, X.-Y. Wang, X.-F. Zhu, Y.-B. Li, Z.-M. Gu, S.-J. Liang, H. Gao, L. Lu, L. Ge, S. Zhang, J. Zhu, R.-M. Ma, Revealing the missing dimension at an exceptional point. *Nat. Phys.* **16**, 571–578 (2020).
5. H. Hodaei, A. U. Hassan, S. Wittek, H. Garcia-Gracia, R. El-Ganainy, D. N. Christodoulides, M. Khajavikhan, Enhanced sensitivity at higher-order exceptional points. *Nature* **548**, 187–191 (2017).
6. L. Chang, X. Jiang, S. Hua, C. Yang, J. Wen, L. Jiang, G. Li, G. Wang, M. Xiao, Parity–time symmetry and variable optical isolation in active–passive-coupled microresonators. *Nat. Photon.* **8**, 524–529 (2014).
7. B. Peng, Ş. K. Özdemir, F. Lei, F. Monifi, M. Gianfreda, G. L. Long, S. Fan, F. Nori, C. M. Bender, L. Yang, Parity–time-symmetric whispering-gallery microcavities. *Nat. Phys.* **10**, 394–398 (2014).
8. C. Wang, W. R. Sweeney, A. D. Stone, L. Yang, Coherent perfect absorption at an exceptional point. *Science* **373**, 1261–1265 (2021).
9. C. Dembowski, H.-D. Gräf, H. L. Harney, A. Heine, W. D. Heiss, H. Rehfeld, A. Richter, Experimental observation of the topological structure of exceptional points. *Phys. Rev. Lett.* **86**, 787–790 (2001).
10. B. Zhen, C. W. Hsu, Y. Igarashi, L. Lu, I. Kaminer, A. Pick, S.-L. Chua, J. D. Joannopoulos, M. Soljačić, Spawning rings of exceptional points out of Dirac cones. *Nature* **525**, 354–358 (2015).
11. J.-H. Park, A. Ndao, W. Cai, L. Hsu, A. Kodigala, T. Lepetit, Y.-H. Lo, B. Kanté, Symmetry-breaking-induced plasmonic exceptional points and nanoscale sensing. *Nat. Phys.* **16**, 462–468 (2020).
12. H. Hodaei, M.-A. Miri, M. Heinrich, D. N. Christodoulides, M. Khajavikhan, Parity-time-symmetric microring lasers. *Science* **346**, 975–978 (2014).
13. Y.-H. Lai, Y.-K. Lu, M.-G. Suh, Z. Yuan, K. Vahala, Observation of the exceptional-point-enhanced Sagnac effect. *Nature* **576**, 65–69 (2019).
14. M. P. Hokmabadi, A. Schumer, D. N. Christodoulides, M. Khajavikhan, Non-Hermitian ring laser gyroscopes with enhanced Sagnac sensitivity. *Nature* **576**, 70–74 (2019).
15. W. Chen, Ş. Kaya Özdemir, G. Zhao, J. Wiersig, L. Yang, Exceptional points enhance sensing in an optical microcavity. *Nature* **548**, 192–196 (2017).

16. H. Xu, D. Mason, L. Jiang, J. G. E. Harris, Topological energy transfer in an optomechanical system with exceptional points. *Nature* **537**, 80–83 (2016).
17. Z. Xu, X. Gao, J. Bang, Z. Jacob, T. Li, Non-reciprocal energy transfer through the Casimir effect. *Nat. Nanotechnol.* **17**, 148–152 (2022).
18. J. Doppler, A. A. Mailybaev, J. Böhm, U. Kuhl, A. Girschik, F. Libisch, T. J. Milburn, P. Rabl, N. Moiseyev, S. Rotter, Dynamically encircling an exceptional point for asymmetric mode switching. *Nature* **537**, 76–79 (2016).
19. H. Xu, L. Jiang, A. A. Clerk, J. G. E. Harris, Nonreciprocal control and cooling of phonon modes in an optomechanical system. *Nature* **568**, 65–69 (2019).
20. S. Barzanjeh, A. Xuereb, S. Gröblacher, M. Paternostro, C. A. Regal, E. M. Weig, Optomechanics for quantum technologies. *Nat. Phys.* **18**, 15–24 (2022).
21. M. Sansa, M. Defoort, A. Brenac, M. Hermouet, L. Banniard, A. Fafin, M. Gely, C. Masselon, I. Favero, G. Jourdan, S. Hentz, Optomechanical mass spectrometry. *Nat. Commun.* **11**, 3781 (2020).
22. H. Xiong, Z.-X. Liu, Y. Wu, Highly sensitive optical sensor for precision measurement of electrical charges based on optomechanically induced difference-sideband generation. *Opt. Lett.* **42**, 3630–3633 (2017).
23. P. H. Kim, B. D. Hauer, C. Doolin, F. Souris, J. P. Davis, Approaching the standard quantum limit of mechanical torque sensing. *Nat. Commun.* **7**, 13165 (2016).
24. Q. Lin, J. Rosenberg, D. Chang, R. Camacho, M. Eichenfield, K. J. Vahala, O. Painter, Coherent mixing of mechanical excitations in nano-optomechanical structures. *Nat. Photon.* **4**, 236–242 (2010).
25. A. B. Shkarin, N. E. Flowers-Jacobs, S. W. Hoch, A. D. Kashkanova, C. Deutsch, J. Reichel, J. G. E. Harris, Optically mediated hybridization between two mechanical modes. *Phys. Rev. Lett.* **112**, 013602 (2014).
26. N. Spethmann, J. Kohler, S. Schreppler, L. Buchmann, D. M. Stamper-Kurn, Cavity-mediated coupling of mechanical oscillators limited by quantum back-action. *Nat. Phys.* **12**, 27–31 (2016).
27. Y.-P. Wang, J. W. Rao, Y. Yang, P.-C. Xu, Y. S. Gui, B. M. Yao, J. Q. You, C.-M. Hu, Nonreciprocity and unidirectional invisibility in cavity magnonics. *Phys. Rev. Lett.* **123**, 127202 (2019).
28. M. Aspelmeyer, T. J. Kippenberg, F. Marquardt, Cavity optomechanics. *Rev. Mod. Phys.* **86**, 1391–1452 (2014).
29. T. J. Kippenberg, K. J. Vahala, Cavity optomechanics: Back-action at the mesoscale. *Science* **321**, 1172–1176 (2008).
30. Y. Choi, C. Hahn, J. W. Yoon, S. H. Song, Observation of an anti-PT-symmetric exceptional point and energy-difference conserving dynamics in electrical circuit resonators. *Nat. Commun.* **9**, 2182 (2018).
31. Y. Li, Y.-G. Peng, L. Han, M.-A. Miri, W. Li, M. Xiao, X.-F. Zhu, J. Zhao, A. Alù, S. Fan, C.-W. Qiu, Anti–parity-time symmetry in diffusive systems. *Science* **364**, 170–173 (2019).
32. P. Peng, W. Cao, C. Shen, W. Qu, J. Wen, L. Jiang, Y. Xiao, Anti-parity–time symmetry with flying atoms. *Nat. Phys.* **12**, 1139–1145 (2016).
33. J. Chan, A. H. Safavi-Naeini, J. T. Hill, S. Meenehan, O. Painter, Optimized optomechanical crystal cavity with acoustic radiation shield. *Appl. Phys. Lett.* **101**, 081115 (2012).
34. M. Eichenfield, J. Chan, R. M. Camacho, K. J. Vahala, O. Painter, Optomechanical crystals. *Nature* **462**, 78–82 (2009).
35. T. J. Johnson, M. Borselli, O. Painter, Self-induced optical modulation of the transmission through a high-Q silicon microdisk resonator. *Opt. Express* **14**, 817–831 (2006).
36. N. Cazier, X. Checoury, L.-D. Haret, P. Boucaud, High-frequency self-induced oscillations in a silicon nanocavity. *Opt. Express* **21**, 13626–13638 (2013).
37. J. Chan, T. P. M. Alegre, A. H. Safavi-Naeini, J. T. Hill, A. Krause, S. Gröblacher, M. Aspelmeyer, O. Painter, Laser cooling of a nanomechanical oscillator into its quantum ground state. *Nature* **478**, 89–92 (2011).
38. I. Shomroni, L. Qiu, D. Malz, A. Nunnenkamp, T. J. Kippenberg, Optical backaction-evading measurement of a mechanical oscillator. *Nat. Commun.* **10**, 2086 (2019).
39. A. H. Safavi-Naeini, T. P. M. Alegre, J. Chan, M. Eichenfield, M. Winger, Q. Lin, J. T. Hill, D. E. Chang, O. Painter, Electromagnetically induced transparency and slow light with optomechanics. *Nature* **472**, 69–73 (2011).
40. J. D. Cohen, S. M. Meenehan, G. S. MacCabe, S. Gröblacher, A. H. Safavi-Naeini, F. Marsili, M. D. Shaw, O. Painter, Phonon counting and intensity interferometry of a nanomechanical resonator. *Nature* **520**, 522–525 (2015).
41. M. J. Burek, J. D. Cohen, S. M. Meenehan, N. El-Sawah, C. Chia, T. Ruelle, S. Meesala, J. Rochman, H. A. Atikian, M. Markham, D. J. Twitchen, M. D. Lukin, O. Painter, M. Lončar, Diamond optomechanical crystals. *Optica* **3**, 1404–1411 (2016).
42. K. Cui, Z. Huang, N. Wu, Q. Xu, F. Pan, J. Xiong, X. Feng, F. Liu, W. Zhang, Y. Huang, Phonon lasing in a hetero optomechanical crystal cavity. *Photon. Res.* **9**, 937–943 (2021).
43. Y. Zhi, X.-C. Yu, Q. Gong, L. Yang, Y.-F. Xiao, Single nanoparticle detection using optical microcavities. *Adv. Mater.* **29**, 1604920 (2017).
44. W. Yu, W. C. Jiang, Q. Lin, T. Lu, Cavity optomechanical spring sensing of single molecules. *Nat. Commun.* **7**, 12311 (2016).
45. F. Pan, K. Cui, G. Bai, X. Feng, F. Liu, W. Zhang, Y. Huang, Radiation-pressure-antidamping enhanced optomechanical spring sensing. *ACS Photon.* **5**, 4164–4169 (2018).
46. F. Massel, S. U. Cho, J.-M. Pirkkalainen, P. J. Hakonen, T. T. Heikkilä, M. A. Sillanpää, Multimode circuit optomechanics near the quantum limit. *Nat. Commun.* **3**, 987 (2012).
47. K. Ding, G. Ma, M. Xiao, Z. Q. Zhang, C. T. Chan, Emergence, coalescence, and topological properties of multiple exceptional points and their experimental realization. *Phys. Rev. X* **6**, 021007 (2016).
48. M. Zhang, G. S. Wiederhecker, S. Manipatruni, A. Barnard, P. McEuen, M. Lipson, Synchronization of micromechanical oscillators using light. *Phys. Rev. Lett.* **109**, 233906 (2012).
49. J. Zhang, B. Peng, Ş. K. Özdemir, K. Pichler, D. O. Krimer, G. Zhao, F. Nori, Y. Liu, S. Rotter, L. Yang, A phonon laser operating at an exceptional point. *Nat. Photon.* **12**, 479–484 (2018).
50. N. Wu, K. Cui, X. Feng, F. Liu, W. Zhang, Y. Huang, Hetero-optomechanical crystal zipper cavity for multimode optomechanics. *Photon.* **9**, 78 (2022).
51. W. P. Bowen, G. J. Milburn, *Quantum Optomechanics* (CRC Press, 2016).
52. M. L. Gorodetsky, A. Schliesser, G. Anetsberger, S. Deleglise, T. J. Kippenberg, Determination of the vacuum optomechanical coupling rate using frequency noise calibration. *Opt. Express* **18**, 23236–23246 (2010).
53. F. Marquardt, J. G. E. Harris, S. M. Girvin, Dynamical multistability induced by radiation pressure in high-finesse micromechanical optical cavities. *Phys. Rev. Lett.* **96**, 103901 (2006).
54. A. G. Krause, J. T. Hill, M. Ludwig, A. H. Safavi-Naeini, J. Chan, F. Marquardt, O. Painter, Nonlinear radiation pressure dynamics in an optomechanical crystal. *Phys. Rev. Lett.* **115**, 233601 (2015).
55. T. Carmon, M. C. Cross, K. J. Vahala, Chaotic quivering of micron-scaled on-chip resonators excited by centrifugal optical pressure. *Phys. Rev. Lett.* **98**, 167203 (2007).
56. W. Li, P. Piergentili, J. Li, S. Zippilli, R. Natali, N. Malossi, G. D. Giuseppe, D. Vitali, Noise robustness of synchronization of two nanomechanical resonators coupled to the same cavity field. *Phys. Rev. A* **101**, 013802 (2020).
57. S. Assawaworrarit, X. Yu, S. Fan, Robust wireless power transfer using a nonlinear parity–time-symmetric circuit. *Nature* **546**, 387–390 (2017).
58. U. Kemiktarak, M. Durand, M. Metcalfe, J. Lawall, Mode competition and anomalous cooling in a multimode phonon laser. *Phys. Rev. Lett.* **113**, 030802 (2014).
59. J. Sheng, X. Wei, C. Yang, H. Wu, Self-organized synchronization of phonon lasers. *Phys. Rev. Lett.* **124**, 053604 (2020).
60. D. Navarro-Urrios, N. E. Capuj, J. Gomis-Bresco, F. Alzina, A. Pitanti, A. Griol, A. Martínez, C. M. Sotomayor Torres, A self-stabilized coherent phonon source driven by optical forces. *Sci. Rep.* **5**, 15733 (2015).

Acknowledgments: We thank Tianjin H-Chip Technology Group Corporation, Innovation Center of Advanced Optoelectronic Chip, Institute for Electronics and Information Technology in Tianjin, Tsinghua University for their fabrication support with electron beam lithography and inductively coupled plasma etching. **Funding:** This work was supported by National Key R&D Program of China contract 2018YFB2200402, National Natural Science Foundation of China grant 91750206, National Natural Science Foundation of China grant 61775115, Beijing Municipal Science Technology Commission Z201100004020010, Beijing National Science Foundation contract Z180012, Beijing Frontier Science Center for Quantum Information, and Beijing Academy of Quantum Information Sciences. **Author contributions:** Conceptualization: N.W. and K.C. Methodology: N.W. Investigation: N.W. and K.C. Supervision: K.C. and Y.H. Writing—original draft: N.W. and K.C. Writing—review and editing: N.W., K.C., Q.X., X.F., F.L., W.Z., and Y.H. **Competing interests:** The authors declare that they have no competing interests. **Data and materials availability:** All data needed to evaluate the conclusions in the paper are present in the paper and/or the Supplementary Materials.

Submitted 4 March 2022
Accepted 19 December 2022
Published 18 January 2023
10.1126/sciadv.abp8892